Original Contributions

# SAXS data analysis of a lamellar two–phase system. Layer statistics and compansion[1]

N. Stribeck

Institut für Technische und Makromolekulare Chemie der Universität Hamburg, Germany

*Abstract:* An analysis of small angle x–ray scattering (SAXS) data from three injection molded poly(ethylene terephthalate (PET) samples is carried out. Two of the samples are annealed at different temperatures. The chosen concept of data analysis is that of Ruland's interface distribution function (IDF) of lamellar two–phase systems. The IDF can be expanded into a series of distance distributions, containing the information on the topological properties of the ensemble of lamellar stacks in the semicrystalline sample.

The paper describes the stepwise refinement of the topological model. The final model is described by only few parameters of physical meaning. It unifies the well–known concepts of an ensemble of non–uniform stacks, finite stack size and one–dimensional paracrystalline disorder in an analytical expression. In order to deduce this expression, the concept of inhomogeneity is (imagine a variation of the long period from stack to stack) is generally treated in terms of "compansion", a suggested superposition principle. Its mathematical equivalent in one dimension is the Mellin convolution.

*Key words:* SAXS — two–phase system — finite lamellar stacks — stacking statistics — PET

## 1 Introduction

A frequently studied type of superstructure in polymers is the lamellar two–phase system. Transmission electron microscopy (TEM) as well as small angle x–ray scattering (SAXS) are common methods of research in this field. While TEM offers the advantage of a local visual impression of the structure, the SAXS method requires appropriate evaluation methods and structure modeling in order to gain information on global parameters which characterize the structure.

Even the restricted objective of only determining the "long period" from the reflection maxima in the SAXS curve is not a simple task, as Reinhold, Fischer and Peterlin [1] have shown. In order to explain deviations from Bragg's law, the authors suggest a special type of asymmetric function to describe the frequency distribution of long periods. Asymmetric distributions of lamellar thicknesses or long periods have several times been considered for lamellar [2–4] as well as for general [5] two–phase systems.

Additionally, taking into account the SAXS line widths, Strobl and Müller [6] conclude that the ensemble of lamellar stacks shows features of an inhomogeneity in the sense that the long period varies from stack to stack. This model has been considered by others [7, 8] and is similar to the concept of line broadening due to a "homogeneous tension distribution" in a polycrystalline solid [9, 10].

If one considers even more features of the scattering curve, the obtainable results become more detailed [11–15]. However, their significance strongly depends on the validity of the structural model adopted for data analysis.

The data evaluation with the least a priori assumptions has been developed by Vonk and Kortleve [16], who study the one–dimensional correlation function, $\gamma_1(r)$. From $\gamma_1(r)$, however, it is not a simple task

[1] typos corrected by the author and reprinted from Colloid Polym Sci 271:1007–1023 (1993)

to extract the essential parameters of the lamellar system (e.g. thickness of the transition zone between the phases, thickness distributions of the lamellae, the statistical law governing the stacking of the lamellae).

A more advanced method has been developed by Ruland [17], who describes the determination of the interface distribution function (IDF), $g_1(r)$, by means of a Fourier transform of an interference function, $G_1(s)$ or $\tilde{G}_1(s)$. It is somewhat laborious to obtain $\tilde{G}_1(s)$ from the measured scattering intensity, whereas for the correlation function method it is, in general, sufficient to subtract a constant background from the measured curve before a Fourier transform is performed. Despite the additional effort associated with the determination of $\tilde{G}_1(s)$, this procedure has two advantages. Firstly, the parameters describing the deviations of a distorted two–phase system from an ideal one have been determined [18], and their effect has been "peeled off", i.e. eliminated in the remaining data set, paying attention to the validity of Porod's law. Secondly, $g_1(r)$, the Fourier transform of the interference function, can easily be expressed in terms of the questioned frequency distributions of the crystalline and amorphous layer thicknesses of an ideal two–phase system. Such an ideal system is defined by only two constant phase densities and sharp domain boundaries.

The above mentioned information peeling principle is the fundamental tool in the present study. It shall be applied repeatedly, until the lamellar superstructure appears to be resolved. Thus a model is successively generated during several steps of data analysis and a theoretical consideration. The question after each step will be, are we able to recognize the model statistics of lamellar arrangement along the stack? If this is not the case, we will have to peel off another shell of information first.

# 2 Experimental and results from associated measurements

## 2.1 Samples and density measurements

Three injection molded PET samples have been prepared. After molding, two of the samples have been annealed for 4 h at different temperatures (240 °C and 248 °C).

The sample dimensions are 40 mm ×10 mm ×2 mm. Thickness variation of the individual sample is small.

The densities of the samples have been measured in a density gradient tube. For the determination, small piecelets of polymer have been cut away, beginning from the upper edge, resulting in nine layers of test pieces covering the whole height of the sample. This procedure has been carried out twice for every sample in two vertical bands, approx. 1 cm from each end of the platelet. The unannealed sample shows an increase of density towards the central axis of the platelet where the SAXS study has been carried out previously. The volume crystallinity, $\alpha_d$, increases from 0.37 at the edges to 0.42 in the center of the sample. The annealed samples are rather brittle, so for these samples it has been impossible to cut intact piecelets ranging from the front to the back side of the sample. This might in part be a reason for the poor statistics and only faint indication of a density increase towards the center, as compared to the unannealed sample. For every sample the highest measured density $\rho$ along the center line of the sample platelet has been used to compute the mean volume crystallinity $\alpha_d$ . Its difference to the lowest density reading along this line is assumed to give the error of determination (cf. Table 1).

Table 1: Injection molded PET samples and their characterization. Annealing temperature $T_a$, thickness $t$, density $\rho$ and volume crystallinity $\alpha_d$, as determined from density measurement using $\rho_a = 1.3379\,\mathrm{g/cm^3}$ and $\rho_c = 1.4895\,\mathrm{g/cm^3}$

| $T_a$ [C] | — | 240 | 248 |
|---|---|---|---|
| $t$ [mm] | $2.35 \pm 0.01$ | $2.15 \pm 0.02$ | $2.21 \pm 0.03$ |
| $\rho\,[\mathrm{g/cm^3}]$ | $1.401 \pm 0.002$ | $1.423 \pm 0.003$ | $1.425 \pm 0.004$ |
| $\alpha_d$ | $0.42 \pm 0.02$ | $0.56 \pm 0.02$ | $0.58 \pm 0.03$ |

## 2.2 X–ray measurements

For all measurements Ni–filtered Cu–$K_\alpha$ radiation has been used. With a pinhole camera, wide–angle X–ray patterns as well as small–angle X–ray patterns have been recorded on photographic film. The recordings from both methods show perfect isotropy and a long period of approx. 10 nm for all three samples.

For quantitative SAXS measurements a Kratky Compact Camera, equipped with proportional counter and energy discriminator has been used. The receiving slit length, $\ell_1$, has been set to an integral length of $2.01\,\mathrm{nm^{-1}}$ in units of the modulus of the scatter-

ing vector $s$ (for definition cf. section 4). At each position of the scattering curve 20000 counts have been accumulated in order to keep the statistical error sufficiently small. Normalization to absolute intensity [19] has been carried out by means of the moving slit method.

Every scattering curve is composed of two sets, recorded with different entrance slit heights (75 $\mu$m and 130 $\mu$m). Slit–height desmearing does not change the chape of the individual sets.

# 3 Data evaluation tools

All data evaluation is carried out on IBM compatible personal computers. Some programs have been developed by the author himself by means of Turbo Pascal 6.0. The sources of these programs are documented in German language.

## 3.1 TOPAS

TOPAS is a computer program for the processing of SAXS data from two–phase systems. Its ultimate capabilities are computation of correlation functions, chord distributions or IDFs. A small handbook in English, and an English and German user interface are available. The minimum hardware platform is a 80286–computer. Hercules graphics or VGA are necessary.

## 3.2 Nonlinear regression analysis

Interface distribution functions are analyzed by means of the Simplex algorithm of Caceci and Cacheris [20]. To estimate the quality of the fit, the program module is extended by several procedures which have been described by Draper and Smith [21]

- Computation of the asymptotic correlation matrix, yielding information on parameter correlation (to avoid overparametrization);
- Computation of the asymptotic intervals of confidence for each parameter value;
- Plot of the estimation error (to avoid underparametrization);
- Plots of data and fitted curve.

Since the computation of some special model functions applied in the present study is time consuming, an 80486 with 33 MHz is recommended. In order to use the different programs successfully, the user must be able to understand and modify object–oriented Turbo–Pascal programs which make extensive use of pointer structures.

## 3.3 Commercial software

Rapid prototyping and visualization in data analysis as well as in theoretical development has been supported by MathCAD 2.5. Mathematica has been used for the verification of theoretical deductions.

# 4 Non–ideal and global aspects of the two–phase system

The extraction of the outer shell of information from the SAXS data sets starts from the absolute, slit–smeared 1D–interference function $\tilde{G}_1(s)$ or, after transformation from reciprocal to physical space, from the IDF $g_1(r)$. The latter functions contain information only on the topology of an ideal two–phase system along the axis normal to the surfaces of the lamellae. $s$ is the modulus of the scattering vector $s = (2/\lambda)\sin\theta$, with $\theta$ being defined as half of the scattering angle. $\lambda = 0.15418\,\mathrm{nm}$ is the wavelength of radiation. $V$ is the irradiated volume of the sample. According to Ruland [17, 18] $\tilde{G}_1(s)$ is defined by

$$\tilde{G}_1(s) = \left(J(s)/V - J_{Fl}\right) s^3 / F(\sigma_z, s) - \tilde{A}_P, \quad (1)$$

with

$$\begin{aligned} F(x) &= \left(1 - 8\pi^2 x^2\right) \operatorname{erfc}(2\pi x) \\ &\quad + 4\sqrt{\pi s}\exp\left(-4\pi^2 x^2\right). \end{aligned}$$

Here, $\sigma_z = d_z/3$, is related to $d_z$, the width of the transition zone between the phases. $J_{Fl}$ is the density fluctuation background, which is assumed to be a constant. $\tilde{A}_P$, the Porod asymptote for the slit–smeared SAXS curve, is the constant governing Porod's law. The term $F(\sigma_z, s)$ corrects for deviations under the slit–smearing operation, caused from a phase boundary which is not infinitesimally sharp, but smeared by a Gaussian distribution with standard deviation $\sigma_z$.

(1) is exact, but cannot be used to obtain $J_{Fl}$ and $d_z$ easily from experimental data. Under the condition that $(\sigma_z s)$ is "not too big" in the region where Porod's

law is valid, Koberstein, Morra and Stein [22] have obtained an approximate solution

$$J(s)/V - J_{Fl} \approx \frac{\tilde{A}_P}{s^3} \exp\left(-38\,(\sigma_z s)^{1.81}\right), \quad (2)$$

which often can serve as a tool to obtain good approximate values for $J_{Fl}$ and $d_z$ directly from a plot $\ln\left(s^3\,J(s)/V - J_{Fl}\right)$ vs. $s^{1.81}$. The procedure to obtain $\tilde{G}_1(s)$ from the scattering intensity first uses (2) to obtain approximate values and second (1). The method has been described elsewhere in detail [23], and can be carried out with the author's computer program TOPAS.

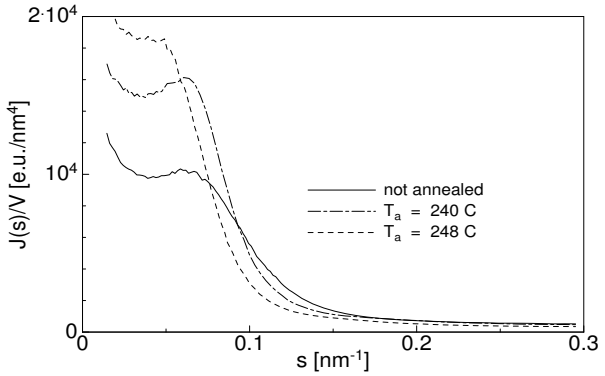


Figure 1: Absolute, smeared SAXS intensity, $J(s)/V$, of three semicrystalline injection molded PET samples recorded with a Kratky camera. Annealing temperatures, $T_a$, are indicated.

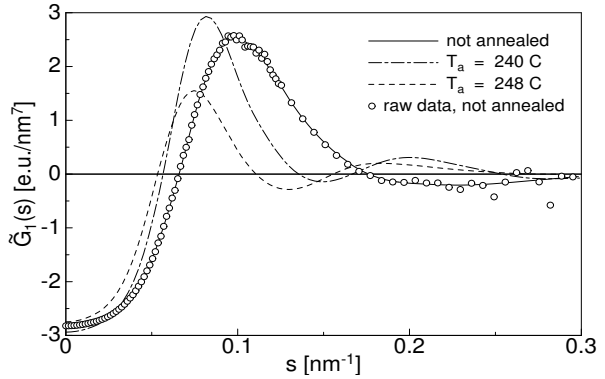


Figure 2: Smeared interference functions, $\tilde{G}_1(s)$, of three injection molded PET samples obtained from $J(s)/V$ after correction for density fluctuations and phase transition zone between the amorphous and crystalline layers. The presented curves have been smoothed by spline functions. One set of raw data is shown in addition.

Fig. 1 shows the absolute SAXS intensity $J(s)/V$ of the three samples. In Fig. 2 the corresponding interference functions, $\tilde{G}_1(s)$, are plotted. The curves are smoothed by means of spline functions. In order to judge the reliability of the splines at large $s$ values, the raw data fro one of the curves have been supplied in addition. Density fluctuation background, $I_{Fl}$, as well as the dimension of the transition zone, $d_z$, describe the deviations from the ideal two–phase system. The values for these parameters are given in Tab. 2. $I_{Fl}$ has been computed from the measured smeared background $J_{Fl}$ using the equation $I_{Fl} = J_{Fl}/\ell_1$ ($\ell_1$ cf. section 2.2). Compared to the rather small long periods, the obtained values of $d_z$ are remarkably high. This means that the approximations which lead to the Koberstein–Morra–Stein plot [22] are not valid. Thus the fluctuation background in the tail of the scattering curve cannot be determined straightforwardly from this plot. The fact becomes evident, as soon as one computes the interference function $\tilde{G}_1(s)$ with the values for $J_{Fl}$ and $d_z$ estimated from the approximative plot and (1). The correction which has to be applied to the estimated values is not small.

Table 2: Injection molded PET samples. Parameters describing the deviations from an ideal two–phase system. Density fluctuation background $I_{Fl}$ and dimension $d_z$ of the transition zone between the phases, as determined from deviations from Porod's law.

| $T_a$ [C] | — | 240 | 248 |
|---|---|---|---|
| $I_{Fl}$ [el/nm$^3$] | $230 \pm 3$ | $201 \pm 3$ | $161 \pm 3$ |
| $d_z$ [nm] | $1.6 \pm 0.2$ | $1.6 \pm 0.2$ | $2.4 \pm 0.2$ |

Table 3: Injection molded PET samples. Invariants of the ideal two–phase system. $\tilde{A}_P$, the asymptote of Porod's law in the slit–smeared SAXS curve. $Q$, the scattering power of the SAXS with respect to the irradiated volume. $\ell_p$, the mean chord length as computed from $\tilde{A}_P$ and $Q$

| $T_a$ [C] | — | 240 | 248 |
|---|---|---|---|
| $\tilde{A}_P$ [el/nm$^8$] | $2.8 \pm 0.1$ | $2.9 \pm 0.1$ | $2.7 \pm 0.1$ |
| $Q$ [el/nm$^6$] | $454 \pm 4$ | $561 \pm 4$ | $495 \pm 4$ |
| $\ell_p$ [nm] | 4.1 | 4.9 | 4.6 |

Fortunately, in the present case, the IDF $g_1(r)$ is found to be very sensitive to the chosen fluctuation background. Only within a small range of values for $J_{Fl}$ no artificial oscillations can be observed in the IDF. Thus, in Tab. 2, those parameter values are listed which minimize these artifacts in the interface distribution function. It must be noted that the chosen method of a constant fluctuation background subtraction may lead to a systematic error for the determined values of $\tilde{A}_P$ and the scattering power. As has been

demonstrated by Wiegand and Ruland [24], the shape of the density fluctuation background should more generally be approximated by a polynomial in even powers of $s$. Moreover, Siemann and Ruland [25] have shown that even small changes in the fluctuation background for a system of SIS block copolymers can result in considerable variation in the Porod asymptote $\tilde{A}_P$.

One observes that the density fluctuation $I_{Fl}$ within the phases decreases as a function of annealing temperature $T_a$, whereas the transition zone $d_z$ between the phases is significantly enlarged for the sample annealed at $248\,^{\circ}C$.

Tab. 4 shows the invariants of the ideal two–phase system, $\tilde{A}_P$, and $Q = 2\pi \int_0^\infty s\,J\,(s)\,/V\,ds$, the scattering power. The mean chord length $\ell_p$ is computed from $\tilde{A}_P$ and $Q$ by means of the equation $\tilde{A}_P = Q/\left(4\pi^2 \ell_p\right)$.

Table 4: Structural model fitting on IDFs from injection molded PET samples. Topological structure parameters of the lamellar stacks according to the fits with free–running variances $\sigma_i$ of the distance distributions $h_i\,(\rho)$ (i.e. on assumptions on the statistical model of lamellar arrangement, but all distance distributions assumed to be Gaussian distributions). For the values of $\sigma_i$ for higher $i$ cf. Fig. 6.

| $T_a$ [C] | — | 240 | 248 |
|---|---|---|---|
| $A_P\,\left[\mathrm{el/nm^8}\right]$ | $1.85 \pm 0.05$ | $2.00 \pm 0.05$ | $1.64 \pm 0.03$ |
| $d_c$ [nm] | $3.5 \pm 0.3$ | $6.4 \pm 0.1$ | $7.1 \pm 0.1$ |
| $d_a$ [nm] | $5.0 \pm 0.1$ | $3.5 \pm 0.3$ | $3.3 \pm 0.3$ |
| $\sigma_c/d_c$ | $0.38 \pm 0.01$ | $0.21 \pm 0.04$ | $0.24 \pm 0.04$ |
| $\sigma_a/d_a$ | $0.34 \pm 0.04$ | $0.44 \pm 0.05$ | $0.67 \pm 0.07$ |
| $\sigma_3/d_3 = \sigma_L/L$ | $0.42 \pm 0.01$ | $0.38 \pm 0.01$ | $0.41 \pm 0.01$ |

According to Ruland [17] the interface distribution $g_1\,(r)$ is computed from $\tilde{G}_1\,(s)$ by the Fourier–Bessel transform

$$g_1\,(r) = \frac{\pi}{4} \int_0^\infty \tilde{G}_1\,(s)\; K\,(2\pi r s)\; ds, \qquad (3)$$

with the kernel $K\,(x)$ being expressed in Bessel functions of the first kind

$$K\,(x) = 3\,(\mathrm{J}_0\,(x) - \mathrm{J}_2\,(x)) + \frac{x}{2}\,(\mathrm{J}_3\,(x) - 3\,\mathrm{J}_1\,(x))\,.$$

The resulting interface distributions of the three samples are shown in Fig. 3. One should bear in mind that the first two peaks (i.e. the first two distance distributions) in the IDF are the distributions of the amorphous and crystalline thicknesses. The curves apparently show that the crystallinity within the lamellar stacks varies as a function of annealing temperature. In order to quantify this result, a model fit on the IDF shall be carried out.

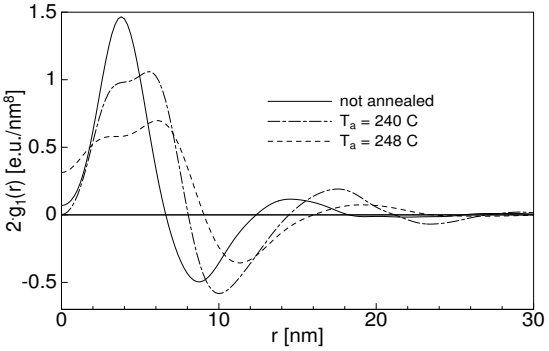


Figure 3: Interface distributions, $g_1\,(r)$, of three injection molded PET samples obtained by Fourier–Bessel transformation of $\tilde{G}_1\,(s)$

# 5 IDF analysis without assumptions on stacking statistics

## 5.1 Considerations concerning the modeling of the IDF

As Ruland [8] has shown, the IDF $g_1\,(r)$ of a lamellar two–phase system can be expanded into a series of distance distributions $h_i\,(r)$

$$g_1\,(r) = A_P \sum_{i=1}^{m} c_i\, h_i\,(r)\,, \qquad (4)$$

with $c_i = 1$ for $i \bmod 3 \neq 0$, and $c_i = -2$ for $i \bmod 3 = 0$. (4) is valid for infinite stack height. Let us number the distance distributions $h_i\,(r)$ in ascending order with respect to their centers of gravity, $d_i$. If we consider a semicrystalline lamellar system with a linear crystallinity $\alpha_\ell > 0.5$, the first distance distribution $h_1\,(r) := h_a\,(r)$ will reflect the distribution of the amorphous layers in the stack. Its center of gravity, $d_1 := d_a$, can be characterized as the average distance between the density alterations at both the surfaces of any amorphous layer. In the same manner $h_2\,(r) := h_c\,(r)$ can be identified as the distribution of crystalline thicknesses, where $d_2 := d_c$ is now the average thickness of the crystalline layers. $h_3\,(r)$ corresponds to the distribution of "long periods", i.e. the distances from the beginning of a crystalline layer to the end of the neighboring amorphous

one (index: $\alpha a$), which should be equal to the distribution of distances from the beginning of an amorphous layer to the end of the neighboring crystalline one (index: $ac$). Thus, $h_3(r) = h_{ca}(r) = h_{ac}(r)$, and $d_3 := L = d_a + d_c$ is the long period.

The subsequent distance distributions can be identified as $h_4(r) := h_{aca}(r)$, $h_5(r) := h_{cac}(r)$, $h_6(r) := h_{caca}(r)$, and $h_7(r) := h_{acaca}(r)$. These seven distance distributions describe the scattering of two crystalline and three amorphous layers from the infinite stack in a consistent manner. If the sub–stack height is increased by a single crystalline lamella, three more distance distribution have to be taken into account. Thus, it is reasonable for the upper limit $m$ of summation in the model to choose $m \in [1, 4, 7, 10, \ldots, \infty]$. Trivially, the center of gravity for every $h_i(r)$ with $i > 2$ can be computed from the centers of gravity $d_1$ and $d_2$ of the first two distance distributions by successive addition.

If one intends to fit the IDF by a model, at least the general type of distance distributions must be fixed. Several studies [1–4] have shown that from experimental findings there may be good reason to assume that the distributions of crystalline thicknesses and long periods are skewed. To the knowledge of the author, the only analytical asymmetric function that has been applied to SAXS data is the Reinhold distribution [1]. Its skew is controlled by its center of gravity and a second parameter $\gamma$. A further asymmetric distribution, which has been proposed by Hanna and Windle [5], is defined by a rather unwieldy product of functions. Moreover, this distribution is not defined for real number arguments, and there is no analytical expression for its center of gravity. Both function types are shown in Fig. 4. The Reinhold distribution shows a typical cut–off at its steep side. If these functions were to be considered as basic functions for modeling the IDF, traces of the cut–off should be observable in IDFs computed from measured data. Such traces have never been found. Thus, if an asymmetric distribution should be considered, it should more likely look similar to the Hanna–Windle distribution.

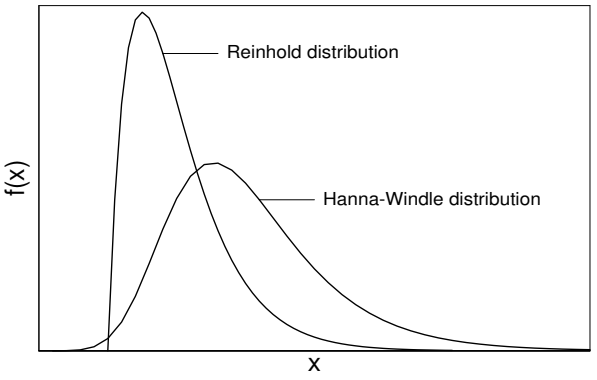


Figure 4: Examples for shapes of asymmetric distributions of thicknesses, as discussed by Reinhold, Fischer and Peterlin [1] as well as Hanna and Windle [5]

If, on the other hand, one tends to assume the distance distribution to be symmetrical about their centers of gravity, it is convenient to propose Gaussian normal distributions $N_i(r, d_i, \sigma_i)$ as a prototype of the distance distributions

$$N_i(r, d_i, \sigma_i) = \frac{1}{\sqrt{2\pi}\sigma_i} \exp\left\{-\frac{1}{2}\left(\frac{r - d_i}{\sigma_i}\right)^2\right\}. \tag{5}$$

Thus, as a first approximation, the model has been generated from (4) and (5) with $m = 13$ and the symmetric Gaussian functions. This model has the disadvantage of a large parameter set, but the advantage that no pre–determinations on the statistics of layer stacking have yet been introduced. Due to the large parameter set, one should be cautious with the interpretation of its results. Nevertheless, the author has frequently used it for the determination of an "infinite linear crystallinity", $\alpha_{\ell\infty}$, which assumes the irradiated volume to be filled with lamellar stacks of infinite height, defined by

$$\alpha_{\ell\infty} = \frac{d_c}{d_a + d_c}, \tag{6}$$

as well as for the determination of the widths of the distributions $h_a(r)$ and $h_c(r)$. It would probably be questionable to discuss the widths of the higher distance distributions in detail. Results on the basis of such a model of "free–running–$\sigma_i$" have been published in several preceding papers [26–28].

Despite the above reservation, the general course of the whole set of parameters shall be used to hint at the mechanism which is most probably determining the statistical arrangement of the ensemble of layer stacks and the lamellae within.

One–dimensional statistics of distances are frequently treated in terms of a model of paracrystalline disorder. If one considers a two–phase system, one can distinguish between a paracrystalline stacking of both types of layer thicknesses and a paracrystalline lattice model, where the lattice constant is subject to paracrystalline disorder, whereas one type of layers decorates the distorted lattice. If one assumes either of these variants to be valid, the number of free width parameters, $\sigma_i$ is reduced to two. The constraining equations for the computation of the other $\sigma_i$ have been presented by Ruland [8]. Here, it is only important that for both paracrystalline models the relation $\lim_{i\to\infty} \sigma_i^2/d_i = \text{const.}$ holds.

A different model for one–dimensional statistics is that of an "inhomogeneous system with exact lattice" (Kratky, cited in Porod [7]), where each stack is assumed to be a perfect lattice with the lattice constant varying from stack to stack. Ruland [8] named this model "homogeneous long period distribution" ("hL–distribution", cf. [9, 10]. For this model the increase of the $\sigma_i$ is limited by the relation $\sigma_i/d_i = \text{const.}$, and a single width parameter determines all other $\sigma_i$.

## 5.2 Results

For the "free–running–$\sigma_i$ model" a part of the parameter set and the corresponding best–fit values are shown in Tab. 4. The specified "asymptotic intervals of confidence" of every parameter value are computed from the parameter correlation matrix according to Draper and Smith [21]. $A_P$ is the fitted integral of the IDF, which should be close to $\lim_{s\to\infty} s^4\, I(s) = Q/\left(2\pi^3 \ell_p\right)$, the Porod asymptote of the unsmeared scattering curve $I(s)$ (of the ideal two–phase system). The following rows in the table specify the average thicknesses of the crystalline and the amorphous layers, respectively, $d_c$ and $d_a$. $d_c$ is identified by means of $\alpha_d$, the crystallinity from density measurement. At the table bottom the relative standard deviations, $\sigma_i/d_i$, for the first three Gaussian distance distributions, $h_i(r)$, are listed. The width parameters of the following distance distributions will be presented in Fig. 6.

Fig. 5 shows an example for the model fit and the decomposition of the corresponding IDF into the series of Gaussian distance distributions.

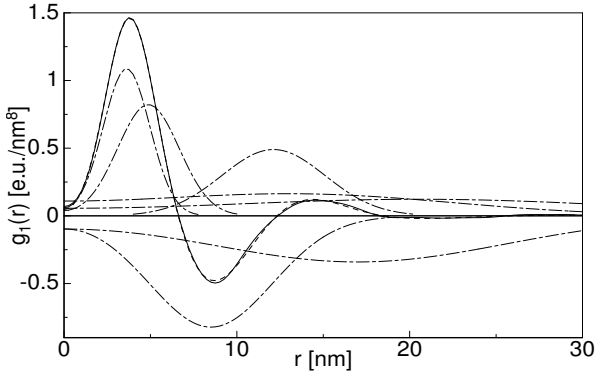


Figure 5: Decomposition of $g_1(r)$ into Gaussian–type distance distributions for the unannealed injection molded PET sample. The width of each Gaussian has been fitted individually by nonlinear regression (Simplex algorithm)

Table 5: Injection molded PET samples. Deduced structure parameters, computed by means of the results of the fit by free–running–$\sigma_i$ and the invariants from Tab. 3. $\alpha_{\ell\infty} := d_c/L$, linear crystallinity; $\Delta\rho_{el} := \sqrt{Q/\left(\alpha_{\ell\infty}\left(1-\alpha_{\ell\infty}\right)\right)}$, the contrast between amorphous and crystalline phase.

| $T_a$ [C] | — | 240 | 248 |
|---|---|---|---|
| $\alpha_{\ell\infty}$ | 0.42 | 0.65 | 0.68 |
| $\Delta\rho_{el}$ $\left[\text{el}/\text{nm}^3\right]$ | 43.2 | 49.5 | 47.8 |

Tab. 5 shows values for deduced parameters, which have been computed in order to discuss and validate the results of the fits. The crystallinity from density, $\alpha_d$ (cf. Tab. 1), and from IDF analysis, $\alpha_{\ell\infty}$, agree only for the unannealed sample. From bulk crystallinity $\alpha$ and scattering power $Q$, one computes the electron density difference, $\Delta\rho_{el}$, between the phases by means of the equation

$$\Delta\rho_{el} = \sqrt{Q/\left(\alpha_{\ell\infty}\left(1-\alpha_{\ell\infty}\right)\right)}. \qquad (7)$$

Assuming that $\alpha_{\ell\infty}$ were the correct bulk crystallinity, one obtains the values presented in the second row of Tab. 5. These values have to be compared to the theoretical contrast, $\Delta\rho_{el} = 47.5\,\text{el}/\text{nm}^3$, which is computed from the mass density difference between the amorphous and crystalline phases (cf. Tab. 1). In particular, the value for the sample annealed at $240\,^{\circ}\text{C}$ is much too high. Thus, $\alpha_{\ell\infty}$, in general, cannot be identified with the bulk crystallinity. A similar result has been obtained in a previous study [23] on different PET samples. In the paper mentioned, we drew the conclusion that "the results favor the view that the lamellar stacks consist of only 3—6 coherently scattering crystal lamellae and there exist amorphous re-

gions outside the lamellar stacks…".

Let us now search for a complete model for the SAXS which has a small set of parameters with physical meaning. Fig. 6 shows the sets of width parameter values, $\sigma_i$, as obtained from the free–running–$\sigma_i$ model fit. The presented plot $\sigma_i^2/d_i$ vs. $d_i$ appears to be appropriate to hint at the strongest principle of lamellar stacking statistics. As mentioned above, any paracrystalline statistics would result in a trend curve with horizontal asymptote. An hL–distribution type of statistics, on the other hand, would be indicated by values following an inclined straight line through the origin — at least for the values from $\sigma_{nL}^2/(nL)$, which correspond to distances of multiples of the long period.

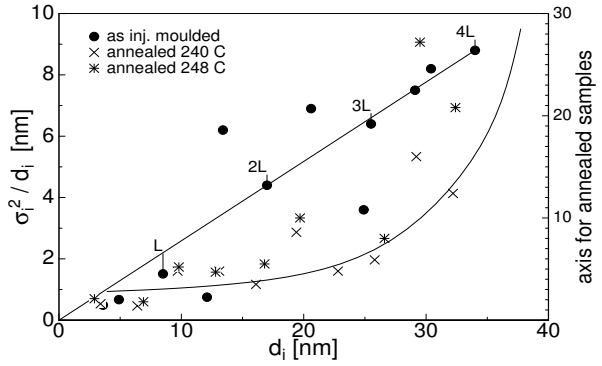


Figure 6: Relative variances $\sigma_i^2/d_i$ of the Gaussian–type distance distributions from a $g_1(r)$ decomposition in fits according to Fig. 5 and Tab. 4. Data are plotted as a function of $d_i$, the position of the $i$–th distribution. Solid lines indicate trends for the unannealed (straight line) and the annealed (increasing curve) PET samples. This plot serves the purpose to discuss probable principles of lamellar stacking statistics

The left y–axis refers to the unannealed sample (filled circles). The trend for this sample appears to warrant further work on the generalization of th hL–distribution's principle. The right y–axis refers to the data of the annealed samples. Here, the loss of correlation is even worse than for the unannealed sample. Such a behavior could be caused from lamellar stacks of finite height The author has plotted width data for several other samples in such test diagrams. A paracrystalline trend has never been found. Sometimes there has been the indication of an hL–distribution, but mostly the trend has been unclear or it has hinted at the presence of finite stacks.

The ideal hL–distribution is completely defined by a single width parameter. But the plots suggest that at least two independent widths should always be incorporated in the model. Therefore, let us try to generalize the principle of the hL–model and peel off the corresponding shell of information from SAXS data.

## 6 Theoretical description of the compansion principle

The ideal hL–model describes the observable structure as a superpositon of perfect 1D–lattices. It is assumed that there exist regions in the sample volume where a common lattice constant can be defined. From region to region this lattice constant is subject to such a variation that every local structure can be generated from an "average local reference structure" by an affine compression or expansion, respectively. This superposition principle of the homogeneous long period distribution ma easily be generalized in order to describe distorted reference structures.

Let $g_{1r}(r)$ be defined as the IDF of the reference stack, which shall describe the average local structure from the ensemble of lamellar stacks. Let $h_H(y)$ be a frequency distribution of compression/expansion factors $y$, which have to be applied to the reference stack in order to generate the ensemble of scattering stacks as a whole. Then $h_H(y)$ describes the heterogeneity of the sample, and the observed IDF, $g_1(r)$, is given by the superposition

$$g_1(r) = \int_0^\infty h_H(y)\,\frac{1}{y} g_{1r}\left(\frac{r}{y}\right) dy. \qquad (8)$$

A well–known integral transform, describing another kind of superposition, is the convolution. It describes the superposition of a function with itself by successive translation in the space of its definition. The convolution is controlled by a second function which can be considered as the frequency distribution of translation factors. (8) describes a different superposition principle in which a function is superimposed by compressed/expanded images of itself. Let us name this principle "compansion". For the present work it is sufficient to consider "1D–compansion", a compansion in one dimension.

### 6.1 Problem reduction. Definition and evident properties of the companion

Since, according to (4) , every IDF can be expanded into the series of the distance distributions $h_i(r)$, the integral transform may be carried out term by term

$$h_i(r) = \int_0^\infty h_H(y)\,\frac{1}{y} h_{ir}\left(\frac{r}{y}\right) dy. \qquad (9)$$

The frequency distribution $h_H(r)$, by definition, is normalized to 1 and its center of gravity is at $r = 1$. By a simple transformation, the same properties can be guaranteed for $h_{ir}(r)$. The necessary transformation combines an affine compression of the $r$–axis and a multiplication by a scalar factor. The remnant problem is of a purely mathematical nature, and involves the study of the integral transform

$$f(r) = \int g(y)\, h\left(\frac{r}{y}\right) \frac{dy}{y} := g(r) \odot h(r) \qquad (10)$$

for the class of functions with norm and mean equal to unity (for definitions also cf. section 6.2), i.e.,

$$\mu'_{0g} = \mu'_{0h} = 1, \qquad (11)$$
$$\mu'_{1g} = \mu'_{1h} = 1 \qquad (12)$$

and $\mu'_{nf}$, the $n$–th moment of the function $f$, being defined by (cf. Zelen and Severo [29, chapter 26])

$$\mu'_{nf} = \int r^n f(r)\, dr, \qquad n \in \mathbb{N}_0. \qquad (13)$$

In mathematical literature (10) is known as known as "*Mellin* convolution"[2]. The relation to the ordinary convolution is readily established by substituting the variables in (10) by their logarithms.

In the same way as the ordinary convolution integral reduces to a simple multiplication upon Fourier or Laplace transformation, a Mellin transformation of (10) results in the product of Mellin transforms

$$F(s) = \mathscr{M}\left(\int_0^\infty g(y)\; h\left(\frac{r}{y}\right) \frac{dy}{y}\right) = G(s)\, H(s), \qquad (14)$$

where the Mellin transformation is defined as

$$F(s) = \mathscr{M}(f(r)) = \int_0^\infty f(r)\; r^{s-1}\, dr, \qquad (15)$$

(see, e.g. Titchmarsh [30, p. 53]. For a complete discussion of the integral (1) see Marichev [31].)

Commutativity $g(r) \odot h(r) = h(r) \odot g(r)$ of the companion can be verified by variable substitution $u := r/y$ in (10). Thus, frequency distribution $h$ and structure distribution $g$ are, in principle, indistinguishable.

### 6.2 Moment series expansion of the companded function

Consider the series of moments of the companded function $f$, as well as that of the operand functions $g$ and $h$. Again, following [29], the $n$–th central moment $\mu_{nf}$ of a function $f$ is defined by

$$\mu_{nf} = \int_{-\infty}^\infty (r - m_f)^n f(r)\, dr, \qquad n \in \mathbb{N}. \qquad (16)$$

Here, $m_f := \mu'_{1f}$ is called the mean of the function $f$. $\sigma_f^2 := \mu_{2f}$ is called its variance. $\gamma_{1f} := \mu_{3f}/\sigma_f^3$ is the skewness of the function and describes its asymmetry. According to Oberhettinger [32, Theorem 4], the Fourier transformed function of $f(r)$, $F(s)$ can be expanded into a series of the moments $\mu'_{kf}$ of $f(r)$

$$F(s) = 1 + \sum_{k=1}^{n} \frac{\mu'_{kf}}{k!} (2\pi i s)^k + \mathrm{O}\left(s^{n+1}\right). \qquad (17)$$

(17) is valid under the premise of the symmetrical definition

$$\mathscr{F}(f(r)) := F(s) := \int_{-\infty}^\infty f(r)\, \mathrm{e}^{2\pi i r s}\, dr \qquad (18)$$

of the 1D–Fourier transformation. According to [29], the central moment $\mu_n$ can be expressed by a series of the moments about origin, $\mu'_j$

$$\mu_n = \sum_{j=0}^{n} \binom{n}{j} (-1)^{n-j}\, m^{n-j}\, \mu'_j. \qquad (19)$$

Rearrangement of (19) yields the inverted relation

$$\mu'_n = m^n + \sum_{j=2}^{n} \binom{n}{j} m^{n-j}\, \mu_j. \qquad (20)$$

[2]The following part of this section cites from the referee's comments to the manuscript, which are gratefully acknowledged by the author.

### 6.3 Transformation of moments under compansion

Apply the moment definition (13) to the definition of compansion, (10) and substitute $u := r/y$. One obtains the theorem

$$\mu'_{nf} = \mu'_{nh} \cdot \mu'_{ng}, \tag{21}$$

i.e., the moments about origin multiply under Mellin convolution. Thus, it follows from (11) and (12) that even the companded function belongs to the class of functions with norm and mean equal to unity. This theorem can as well be deduced from (14) due to the obvious relation between the Mellin transformation and the moments of a distribution.

### 6.4 The second moment of the companded function

Using (20) and (21) for functions from the mentioned class one obtains for the second moment $\mu'_{2f}$ of the Mellin convoluted function $f$

$$\mu'_{2f} = \left(\sigma_g^2 + 1\right)\left(\sigma_h^2 + 1\right), \tag{22}$$

and thus for the second central moment, $\sigma_f^2$, of $f$

$$\left(\sigma_f^2 + 1\right) = \left(\sigma_g^2 + 1\right)\left(\sigma_h^2 + 1\right). \tag{23}$$

### 6.5 The third moment of the companded function. Asymmetry

For the computation of the third moment, $\mu'_{3f}$, let the operand functions $g$ and $h$ be symmetric, i.e., their third central moment shall vanish

$$\mu_{3g} \equiv \mu_{3h} \equiv 0.$$

Then for $\mu'_{3f}$, it follows from Theorem (21)

$$\mu'_{3f} = \left(3\sigma_g^2 + 1\right)\left(3\sigma_h^2 + 1\right), \tag{24}$$

and with (20) and (23) we obtain for the third central moment $\mu_{3f}$ of the companded function $f(r)$

$$\mu_{3f} = 6\,\sigma_g^2\,\sigma_h^2. \tag{25}$$

Thus, $f(r)$, the compansion of the symmetric function $g$ with the symmetric function $h$ is asymmetric, in general. For its skewness $\gamma_{1f}$ it follows

$$\gamma_{1f} = \frac{6\,\sigma_g^2\,\sigma_h^2}{\left(\sigma_g^2 + \sigma_g^2\sigma_h^2 + \sigma_h^2\right)^{3/2}}. \tag{26}$$

### 6.6 Gaussian distributions under compansion

Now assume that $g(r)$ as well as $h(r)$ are normalized Gaussian distributions according to (5). The central moments of Gaussians are well–known definite integrals

$$\mu_n\left(N(r,\sigma,1)\right) = \begin{cases} \frac{\left(\sqrt{2}\sigma\right)^n}{\sqrt{\pi}}\Gamma\left(\frac{n+1}{2}\right) & \text{for } n = 2k \\ 0 & \text{for } n = 2k+1 \end{cases}.$$

Using the notation of the "double factorial" $n!! = n(n-2)(n-4)\ldots 1$ the $\Gamma$–function can be simplified to yield

$$\mu_n\left(N(r,\sigma,1)\right) = \sigma^n\ (n-1)!! \quad \text{for } n = 2k. \tag{27}$$

With this background, one may recursively compute all the moments of the compansion of two Gaussians and thus obtain the power series of $F(s)$ (cf. (17)).

### 6.7 Fourier transformation of the companded function

The Mellin convolution (1D–compansion) from two Gaussians does not lead to a simple analytical solution. In general, extensive tables of Mellin transforms [31, 33] can be used in order to calculate Mellin convolutions or to choose model distributions for which a simple analytical solution exists. But the properties of compansion are such that it appears to be promising to search for an analytical $F(s)$, the Fourier transform of the compansion.

Let $F(s)$ be the 1D–Fourier transformation of the companded function $f(r)$ (cf. (18)), then from the reciprocity theorem of Fourier transformation theory,

$$\mathscr{F}\left(\frac{1}{y}\,f\!\left(\frac{r}{y}\right)\right) = F(ys), \tag{28}$$

it follows that

$$\begin{aligned} F(s) &= \int h(y)\,G(ys)\,dy \\ &= \int H(ys)\,g(y)\,dy. \end{aligned} \tag{29}$$

Here, $H(s)$ designates the 1D–Fourier transform of $h(r)$; $G(s)$ and $g(r)$ correspond in analogous manner. Now let $h(r)$ and $g(r)$ be represented by Gaussians with norm and mean equal to unity. We then obtain for the Mellin convolution in reciprocal space

$$\begin{aligned} F(s) &= \int h(y) \exp\left(-2\pi\sigma_g^2 y^2 s^2\right) \exp(2\pi i y s)\, dy \\ &= \frac{1}{\sqrt{2\pi}\sigma_h} \int \exp\left(-\frac{1}{2}\left(\frac{y-1}{\sigma_h}\right)^2\right) \\ &\quad \times \exp\left(-2\left(\pi\sigma_g y s\right)^2\right) \exp(2\pi i y s)\, dy. \end{aligned}$$

This integral is soluble. After simplification, completion of the quadratic form, and variable substitution, the problem can be reduced to the integration of $\exp\left(-u^2\right)$, and one finally obtains

$$\begin{aligned} F(s) &= \sqrt{A(s)} \exp\left(-A(s) B(s)\right) \exp\left(2\pi i s A(s)\right) \\ &= \sqrt{A(s)} \exp\left(-A(s) B(s)\right) \left[\cos\left(2\pi s A(s)\right)\right. \\ &\quad \left. + i \sin\left(2\pi s A(s)\right)\right] \end{aligned} \tag{30}$$

with

$$A(s) = \frac{1}{1 + \left(2\pi\sigma_g\sigma_h s\right)^2} \tag{31}$$

$$B(s) = 2\pi^2\left(\sigma_g^2 + \sigma_h^2\right) s^2. \tag{32}$$

Compansion's commutativity is reflected in the result.

It has therefore been demonstrated that the compansion may be solved analytically in reciprocal space. Since no analytical expression has been found in real space, reciprocal space data have to be transformed to real space via numerical Fourier transformation. A high accuracy algorithm is the "fast Fourier transformation" (FFT), which can be fed with convenient reciprocal space data, so that it produces the results at precisely the positions where they are needed.

For application in SAXS data analysis, one may identify $\sigma_h \equiv \sigma_H$, the heterogeneity of the ensemble of stacks. In this case $\sigma_g \equiv \sigma_i/d_i$ is the relative standard deviation of the $i$–th distance distribution.

Fig. 7 shows examples for the compansion of two Gaussians. The heterogeneity parameter $\sigma_H$ is varied from 0 to 1. The upper drawing shows compansion in real space. The pure Gaussian for $\sigma_H = 0$ and the increasing asymmetry as heterogeneity grows shall be pointed out. The lower drawing shows the same curves before Fourier transformation. In reciprocal space the companded functions $-F(s)$ are presented with negative sign, in order to make the relation to the unsmeared interference function $G_1(s)$ more suggestive. Only the branch for positive $s$ is shown, since our problem is dealing with even functions only. Thus for application in SAXS data analysis, we omit the imaginary part in (30), but double the weight of $F(s)$.

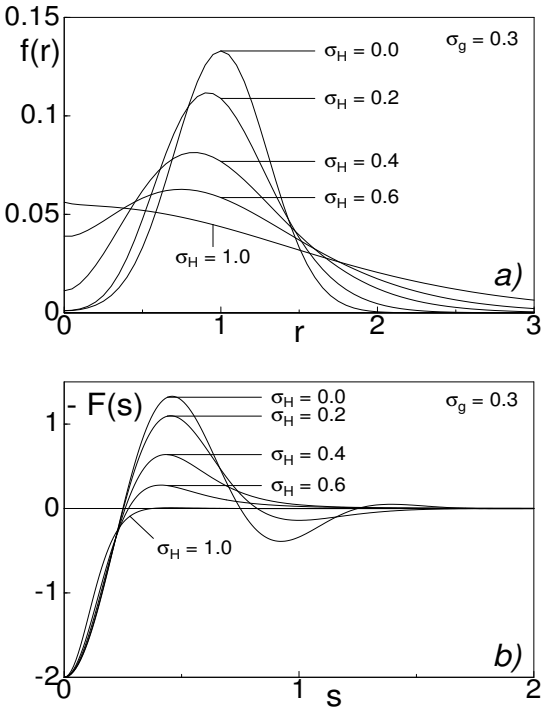


Figure 7: Examples for the Mellin convolution (1D–compansion) of two Gaussians with mean and norm equal to unity. The width parameter of the first Gaussian is $\sigma_g = 0.3$. Only the width parameter of the second Gaussian, $\sigma_H$, takes different values between 0 and 1. a) the compansion $f(r)$ in physical space. b) $-F(s)$, the negative Fourier transform of the compansion $f(r)$. Functions in both diagrams are even $[f(r) = f(-r), \quad F(s) = F(-s)]$

A computer program for the computation of companded functions on the basis of two Gaussian operands is available from the author.

# 7 Results from compansion based IDF analysis

Having the compansion approach at hand, it would be easier to fit the unsmeared interference function $G_1(s)$ than to fit $g_1(r)$, because for the first function all terms are analytical. In this case one would avoid repeated computation of the FFT in each regression step. But since the author is not able to handle a

desmearing which will result in a confidential $G_1(s)$, the following results have been obtained from fits on the IDF as well.

Let us repeat a free–running–$\sigma_i$ model fit, where the distance distributions are not simple Gaussians any more, but companded distributions from a Gaussian heterogeneity distribution $h_H(r)$ and mean local reference distributions $h_{ir}(r)$. Again, the intention is to obtain information on the statistics of layer stacking — now for the assumed local stacks.

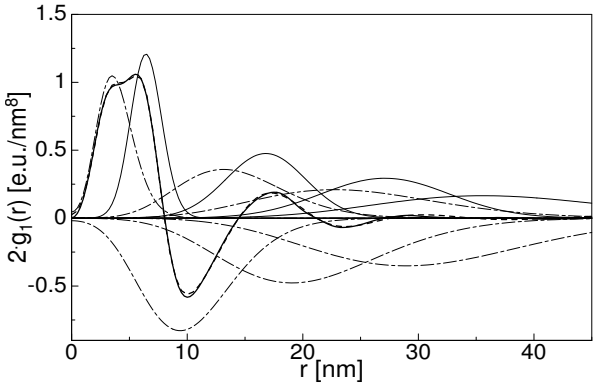


Figure 8: Decomposition of $g_1(r)$ into compansion–type distance distributions for the injection molded PET sample annealed at 240 °C. Heterogeneity, $\sigma_H$, as well as the width of each local Gaussian, $\sigma_i$. have been fitted individually by nonlinear regression (Simplex algorithm)

The results for the annealed samples show a remarkable property, which is presented in Fig. 8. The diagram illustrates the corresponding decomposition into the global distance distributions, $h_i(r)$, which are companded functions. On now observes the asymmetry in the negative peaks, which are the multiples of the long periods. But, more striking, the distance distribution which range between outer edges of crystallites are almost symmetric (thin solid lines; $h_2 \equiv h_c$, $h_5 \equiv h_{cac}$, $h_8 \equiv h_{cacac}$). In other words, the local distributions of these distances are rather narrow. Since the distance distributions in between are considerably wide, we have to conclude that the annealed samples contain lamellar stacks of finite height.

# 8 Determination of an appropriate model for finite stacks by means of nonlinear regression analysis

If one intends to deal with finite stack systems, three questions arise. First, it is important to ask for the distribution of cluster heights. Second, one would like to find an appropriate model for the description of the cluster's border zone, in which the correlation is lost. And third, it is necessary to determine a suitable model for the statistics of lamellar arrangement within the clusters. These questions have been studied by model variation, fit on the experimental IDFs, and comparison of the fit quality.

## 8.1 The distribution of cluster heights

For the study of the distribution of cluster heights a vast model has been composed. Both paracrystalline stacking as well as a lattice with paracrystalline disorder have been checked in parallel fits. Both models assume that every cluster height from 1 (crystalline lamella without correlation) to a cluster of $n$ crystalline lamellae is present with individual weights. The result of this test is that the weights are a function of the chosen $n$, but all weights except 3 are negligible. These 3 weights always belong to adjacent cluster heights. Thus in the next step the complexity of the model is reduced by assuming that the distribution of cluster heights can be described by a Gaussian envelope. This model results an an extremely narrow Gaussian envelope. Thus it should be allowed to consider stacks of a single stack height only.

## 8.2 Models for the cluster border

All the preceding modeling has been carried out under the assumption that no border zone contributes to the scattering. Now, with the finite stack model of a single stack height, 4 model variants have been tested.

Sketches of these models are shown in Fig. 9. Fig. 9a shows a stack with the outer correlated zones being crystalline. In Fig. 9b the outer correlated zones of the stack are amorphous. For all samples model (b) fits better than model (a) (by at least 20% what the residual sum of squares (RSS) is concerned).

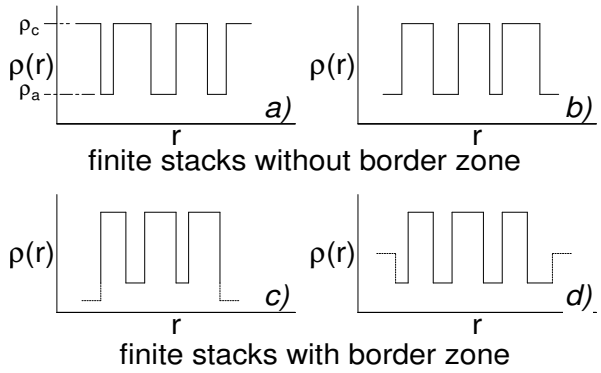


Figure 9: Sketches of models for finite stacks without and with border zone. The best fits on $g_1(r)$ result from model d), a stack composed of $n_L$ crystalline, $n_{L+1}$ amorphous layers and some diffuse border zone

The border zone for the models in the lower row has been introduced by defining an additional layer with average thickness, thickness distribution and contrast of its own. Model (c) with some excess contrast shows severe convergence problems. Model (d) proves to be the best fitting model of all. But even here fit quality estimation of the regression analysis tells that only one of the additional parameters ($\sigma_b$, the standard deviation of the border zone thickness) is a parameter of some evidence, whereas average thickness and contrast obtain values without confidence. As a consequence the border zones thickness has been fixed at a constant value of 1 nm, and the contrast has been given half the contrast between $\rho_c$ and $\rho_a$. Since these settings for the border zone are artificial, the effect of the border zone term to the scattering curve shall be given particular attention in section 9. It will turn out that, indeed, this term is indeterminate do to the inherent insensitivity of the interference function at small $s$.

## 8.3 Statistics with paracrystalline disorder: Stack vs. lattice

Tab. 6 shows the parameter set of the model fit with this finals model for paracrystalline stacking statistics, which is the best choice for all samples. The heterogeneity, $\sigma_H$, of the system of lamellar stacks is almost constant for the three samples. The average crystalline thickness increases with annealing temperature, whereas its standard deviation with respect to the local stacks vanishes. Thus, in the annealed samples the few crystalline lamellae within a finite local stack are of approximately the same thickness, while the thicknesses of the amorphous interlayers from these local stacks vary by 40% and more.

Table 6: Structural model fitting on IDFs from injection molded PET samples. Topological structure parameters of the lamellar stacks according to the results of the fits by the final compound model

| $T_a$ [C] | — | 240 | 248 |
|---|---|---|---|
| $A_P$ $\left[\text{el}/\text{nm}^8\right]$ | $1.74 \pm 0.03$ | $1.77 \pm 0.03$ | $1.64 \pm 0.02$ |
| $\sigma_H$ | $0.21 \pm 0.01$ | $0.24 \pm 0.01$ | $0.24 \pm 0.01$ |
| $d_c$ [nm] | $4.3 \pm 0.1$ | $6.5 \pm 0.1$ | $7.2 \pm 0.1$ |
| $d_a$ [nm] | $4.7 \pm 0.1$ | $4.0 \pm 0.3$ | $3.9 \pm 0.3$ |
| $\sigma_c/d_c$ | $0.26 \pm 0.01$ | $0.02 \pm 0.11$ | $0.04 \pm 0.03$ |
| $\sigma_a/d_a$ | $0.41 \pm 0.01$ | $0.40 \pm 0.03$ | $0.66 \pm 0.0$ |
| $n_L$ | $10 \pm 5$ | $5 \pm 1.4$ | $4 \pm 0.5$ |
| $\sigma_b$ [nm] | $6.5 \pm 2.4$ | $2.5 \pm 1.5$ | $3.5 \pm 0.4$ |
| $\alpha_\ell$ | $0.45 \pm 0.03$ | $0.57 \pm 0.03$ | $0.59 \pm 0.03$ |

The average thickness of the amorphous layers themselves decreases with increasing annealing temperature. Due to compansion, the global distribution of amorphous layers is rather asymmetric, whereas for the crystalline lamellae this is only true for the unannealed sample. For the latter, the stack height $n_L$ is rather high. $n_L$ is the number of complete long periods which belong to a single stack of correlated lamellae. With a stack height of between 5 and 15 crystalline lamellae, a model of infinitely extended stacks should result in a proper fit as well. This is not the case with the annealed samples. Here, the stack height is truly finite. For the computation of the linear crystallinity, $\alpha_\ell$, this means that the contribution of the additional amorphous layer "from the other end of the stack" is not negligible. Thus, for finite stacks, $\alpha_\ell$ must be computed from the equation

$$\alpha_\ell = \frac{n_L\, d_c}{n_L\, d_c + (1 + n_L)\, d_a}. \tag{33}$$

The corresponding values are given in the bottom row of Tab. 6, and now the agreement with the crystallinity from density, $\alpha_d$, is good. Thus, for the present samples it has been demonstrated that the discrepancies between bulk crystallinity and linear crystallinity have to be ascribed to the existence of lamellar stacks of finite height which are embedded in the amorphous matrix.

Since for the unannealed sample the agreement between the bulk and the infinite linear crystallinity has been perfect, and, moreover, the stack height is high, fits with different infinite models have been carried out as well. The results are presented in Fig. 10. The worst fit shown is that with purely paracrystalline

stacking statistics which does not consider compansion. If compansion is considered in addition, RSS is decreased by a factor of 31. The fit which considers a finite stack height (but is not shown in the figure) is only slightly better (RSS = 0.0038). Assuming companded paracrystalline lattice statistics, the fit quality decreases by almost a factor of two as compared to paracrystalline stacking statistics. This result is representative for all three samples. Thus lattice statistics can be excluded.

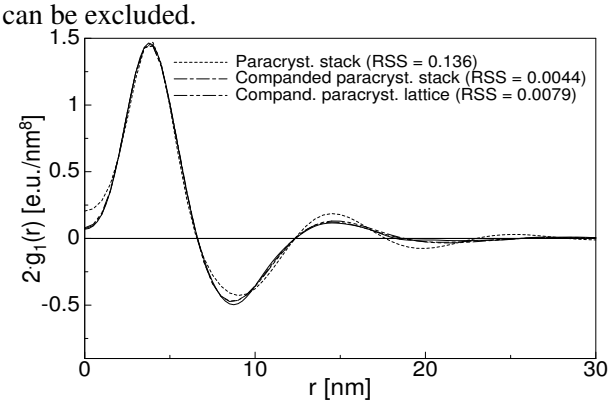


Figure 10: Results from fits with different statistical models for the unannealed PET sample, for which the stack height is close to infinity. RSS is the residual sum of squares. Solid line: Measured interface distribution, $g_1(r)$. Fine dashed line: Paracrystalline stacking with infinite stack height. Dash–dotted line: Paracrystalline stacks of infinite height under compansion. Dash–dot–dotted line: Paracrystalline lattices of infinite height under compansion, with the crystalline layers decorating the distorted lattice

# 9 Synthesis of the scattering curves from the model data

Compansion is an analytical function in reciprocal space. This means that for the suggested model the desmeared interference function, $G_1(s)$, is analytical and can be expressed by

$$G_1(s) = G_{1b}(s) + G_{1s}(s), \tag{34}$$

where $G_{1b}(s)$ characterizes the contribution of the border zones, and $G_{1s}(s)$ is the main contribution originating from the correlation among the crystalline and amorphous layers of the finite stacks

$$G_{1s}(s) = \frac{A_P}{n_L} \sum_{n=1}^{2} \sum_{i=1}^{k+n} C_i \, F_d(\sigma_g, \sigma_H, s). \tag{35}$$

Here $C_i$ is a weighting factor and will be explained in the following. $F_d(\sigma_g, \sigma_H, s)$ is the Fourier transform of a companded function, which is related to a distance between two phase boundaries in the finite stack. These phase boundaries enclose a sub–stack of one or more layers. $i$ is the number of layers in the sub–stack. The accumulation for $n = 1$ concerns those sub–stacks beginning with a layer of "type–1", and for $n = 2$ the sub–stacks starting from a layer of "type–2" are accumulated. Type 2 is the phase which forms both the outer layers of the finite stack. With respect to the present study, it can be identified as the phase of the amorphous layers. $k+2$ is the total number of layers which exist in a finite stack built from $n_L$ layers of type–1, thus, $k = \text{round}(2\,n_L) - 1$. $C_i$ is the frequency with which a sub–stack is found inside the finite stack. This sub–stack begins with type–$n$ and contains $i$ layers. Sub–stacks with an odd number of participants obtain negative sign

$$C_i = (-1)^i \, (n_L + 1 - (i + 2 - n) \text{ div } 2).$$

The operators round and div return the integer fractions of rounding and division, respectively. $\sigma_i$ is the standard deviation of the local Gaussian distance distribution computed from width parameters $\Sigma_1$ and $\Sigma_2$, according to the paracrystalline stacking statistics. Here $\Sigma_1 = \sigma_c$ is the standard deviation of the local distribution of crystalline (i.e. type–1) layers. $\Sigma_2$ is identified with $\sigma_a$ and for the variances of the sub–stack distance distributions we obtain

$$\sigma_i^2 = ((i+1) \text{ div } 2) \; \Sigma_n^2 + (i \text{ div } 2) \; \Sigma_{3-n}^2.$$

The average distance between bottom and top of the sub–stack, $d_i$ follows from

$$d_i = ((i+1) \text{ div } 2) \; D_n + (i \text{ div } 2) \; D_{3-n},$$

where assignment $D_1 = d_c$ and $D_2 = d_a$ is made in analogy to the preceding definition. The Fourier transform of the compansion is computed using the heterogeneity $\sigma_h = \sigma_H$ and applying the transformation rules from section 6.1. In these rules we set $\sigma_g = \sigma_i / d_i$, the relative standard deviation, and compress the $s$–scale by the factor $d_i$. It thus follows that

$$F_d(\sigma_g, \sigma_h, s) = 2\,\Re\left(F(d_i s)\right),$$

which is double the real part from (30).

In a similar way the border term has been defined by

$$G_{1b}(s) = \frac{A_P}{n_L}\left(\sum_{i=2}^{k+3} C_i F_d(\sigma_g, \sigma_H, s) + F_t(s)\right). \tag{36}$$

Here, $F_t(s)$ is related to the form factor of the total finite stack including the border zones, but with only half the contrast. The variables in the sum are now defined differently by

$$\begin{aligned} C_i &= (-1)^i, \\ \sigma_i^2 &= \Sigma_3^2 + (i \text{ div } 2)\,\Sigma_2^2 + ((i-1) \text{ div } 2)\,\Sigma_1^2, \\ d_i &= D_3 + (i \text{ div } 2)\,D_2 + ((i-1) \text{ div } 2)\,D_1, \end{aligned}$$

with $D_3 = 0.1\,\text{nm}$ fixed and small. $\Sigma_3 = \sigma_b$ is the model parameter for the standard deviation of the local border zone.

Fig. 11 shows the decomposition of $G_1(s)$ into the terms $G_{1b}(s)$ and $G_{1s}(s)$ for the unannealed sample. The thin dashed curves demonstrate the compansion $H_c(s)$ of the global distribution of crystalline thicknesses and $H_a(s)$, which in similar manner corresponds to the amorphous layer distribution.

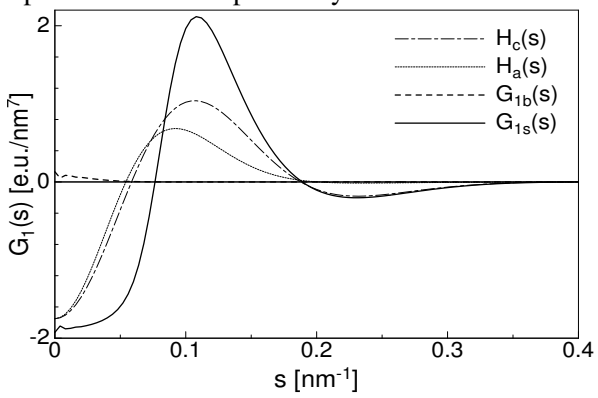


Figure 11: Components of the model from the best fit of the unannealed PET sample, presented in terms of the unsmeared interference function, $G_1(s)$, the Fourier transform of $g_1(r)$ with negative sign. $H_c(s)$, $H_a(s)$: Form factors of the crystalline lamellae and from the amorphous lamellae, respectively. $G_{1b}(s)$: Stack–border term in $G_1(s)$. $G_{1s}(s)$: Stack–without–border term of the finite stack in $G_1(s)$

Obviously, the $G_{1b}(s)$–term is only significant for small values of $s$, where the interference function is rather insensitive due to the multiplication of the scattering intensity by $s^4$. Thus, the effect of the border term should only be regarded as some correction term with low physical meaning.

The next step in data synthesis is the multiplication of $(G_1(s) + A_P)$ by $s^{-4}$ in order to obtain the desmeared scattering curve, $I(s)/V$, of the ideal two–phase system. The synthesized curves are presented in Fig. 12. Utilizing the equation

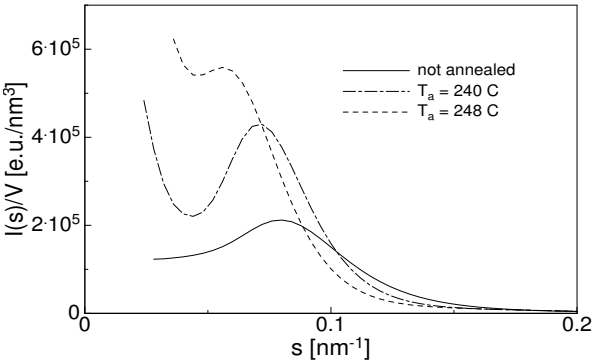


Figure 12: Synthesis of the unsmeared scattering curves, $I(s)/V$, from the synthetic $G_1(s)$ curves computed from the parameter sets retrieved from the best model fits on the IDFs from measurement.

$$J(s)/V \approx I_{Fl}\,\ell_1 + \int_0^{s_{max}} I\left(\sqrt{s^2+y^2}\right)/V\,dy, \tag{37}$$

one can approximately generate the smeared scattering intensity by numerical integration and compare it to the raw measured data. $s_{max} = 0.4\,\text{nm}^{-1}$ is the upper limit, up to which the model function has been computed. The computation neglects the effect of a finite width of the phase transition zone, $d_z$, which, with respect to the chosen plot, will lead to very small systematic deviations in the tail of the curves. Fig. 13 shows the results.

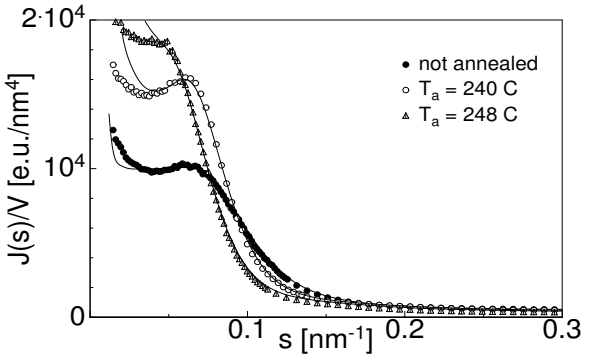


Figure 13: Smeared scattering curves $J(s)/V$ synthesized from IDF model fits obtained by numerical smearing of the curves in Fig. 12 and subsequent

background addition compared to the initial measured data from 3 injection molded PET samples

From a lower limit of $s_{min} \approx 0.07\,\mathrm{nm}^{-1}$ the model functions fit the original data. According to the preceding considerations, the region for $s < s_{min}$ may be dominated by the nature of the loss of correlation in the border zone of the finite lamellar stacks. To study this zone, fits of the interference function or on the IDF are not appropriate, since these functions are insensitive to considerable changes of the raw data at small values of $s$, the modulus of the scattering vector.

## 10 Conclusion

This study shows that the frequently discussed models for the statistics in an ensemble of lamellar stacks may be superimposed. This superposition results in a data set which, in fact, agrees with none of the pure models. The novel compound model proposed in this study considers the principles of compansion, finite stack height, and one–dimensional paracrystalline disorder. It is able to describe a wide range of distorted two–phase structures. The model comprises a small parameter set of only eight parameters, seven of which have physical meaning. As has been shown, the SAXS curve can be synthesized by means of the analyzed parameter values from the model fit. The deviations between measured intensity and model intensity at the beginning of the curve may be related to a not yet understood principle which describes the loss of correlation at the border of finite stacks of lamellae. Some of the deviations between both curves may, in addition, result from the coarse approach to synthesis of scattering intensity since integration has been carried out by summation over a finite range only.

Asymmetric distributions of long periods or thicknesses of lamellae have been discussed in the literature. This study has shown that such asymmetry is inherent to the compansion principle, which has been proposed here in a theoretical treatment. In the deduced form, the compansion may be applied to structures which are of one–dimensional nature, such as the analyzed lamellar systems or fibrillar two–phase systems, e.g. certain thermoplastic elastomers in the elongated state. A generalization of the compansion integral transform to three dimensions has not been attempted.

Compansion may not be a general principle of distorted two–phase systems, but it should be taken into consideration. Its presence may be investigate by means of the presented data evaluation method.

**Acknowledgments.** I am indebted to Prof. F. J. Baltá Calleja, Madrid, and to Prof. L. Mandelkern, Tallahassee, for different sets of different samples which gave the last impulse for the development of compansion theory. I gratefully acknowledge the preparation of the PET test samples by Dr. R. K. Bayer, Kassel and the stimulation of this study by Prof. H. G. Zachmann. Special thanks to Ms. U. Dambeck for carrying out measurements with the pinhole camera and for preparing the density gradient.

## References

[1] Reinhold C, Fischer EW, Peterlin A (1964) J Appl Phys 35:71

[2] Hall IH, Mahmoud EA, Carr PD, Geng YD (1987) Colloid Polym Sci 265:383

[3] Strobl GR, Schneider MJ, Voigt-Martin IG (1980) J Polym Sci Part B Polym Phys B18:1361

[4] Voigt-Martin IG, Mandelkern L (1989) J Polym Sci Part B Polym Phys B27:967

[5] Hanna S, Windle AH (1988) Polymer 29:207

[6] Strobl GR, Müller N (1973) J Polym Sci Part B Polym Phys 11:1219

[7] Porod G (1951) Kolloid Z 124:83

[8] Stribeck N, Ruland W (1978) J Appl Cryst 11:535

[9] Dehlinger U, Kochendörfer A (1939) Z Kristallograf 101:134

[10] Kochendörfer A (1944) Z Kristallograf 105:438

[11] Tsvankin DY, Zubov A, Kitaigorodskii AI (1968) J Polym Sci Part C 16:4081

[12] Strobl GR (1973) J Appl Cryst 6:365

[13] Brämer R (1974) Colloid Polym Sci 252:504

[14] Kilian HG, Wenig W (1974) J Macromol Sci Phys B9:463

[15] Shibayama M, Hashimoto T (1986) Macromolecules 19:740

[16] Vonk CG, Kortleve G (1967) Kolloid Z u Z Polymere 220:19

[17] Ruland W (1977) Colloid Polym Sci 255:417

[18] Ruland W (1971) J Appl Cryst 4:71

[19] Polizzi S, Stribeck N, Zachmann HG, Bordeianu R (1989) Colloid Polym Sci 267:281

[20] Caceci MS, Cacheris WP (1984) Byte 1984:340

[21] Draper NR, Smith H (1980) Applied Regression Analysis, Second Edition. John Wiley & Sons, New York

[22] Koberstein JT, Morra B, Stein RS (1980) J Appl Cryst 13:34

[23] Santa Cruz C, Stribeck N, Zachmann HG, Baltà Calleja FJ (1991) Macromolecules 24:5980

[24] Wiegand W, Ruland W (1979) Progr Colloid Polym Sci 66:355

[25] Siemann U, Ruland W (1982) Colloid Polym Sci 260:999

[26] Stribeck N (1989) Colloid Polym Sci 267:301

[27] Stribeck N, Bösecke P, Polizzi S (1989) Colloid Polym Sci 267:687

[28] Stribeck N (1992) Colloid Polym Sci 270:9

[29] Abramowitz M, Stegun IA (eds.) (1968) Handbook of Mathematical Functions. Dover Publications, New York

[30] Titchmarsh EC (1948) Introduction to the theory of Fourier integrals. Clarendon Press, Oxford

[31] Marichev OI (1983) Handbook of Integral Transforms of Higher Transcendental Functions. Ellis Horwood Ltd., Chichester

[32] Oberhettinger F (1973) Fourier Transforms of Distributions and Their Inverses – A Collection of Tables. Academic Press, New York

[33] Oberhettinger F (1974) Tables of Mellin Transforms. Springer, Berlin

Received September 30, 1992;
accepted December 2, 1992

Author's address:
Dr. N. Stribeck
Universität Hamburg
Institut TMC
Bundesstr. 45
D–20146 Hamburg
Germany